

led system, leaving behind a deficit of N_2O , equivalent to 0.0013 Tg of N emitted at the surface.

The rise in atmospheric N_2O over the last century, presumably due to human activities such as the use of fixed nitrogen in fertilizers (6), has changed the atmosphere and the budget of N_2O . The photochemical coupling of the $\{N_2O, NO_y, O_3\}$ -system that makes perturbations to N_2O decay faster than the steady-state loss rate also implies that the N_2O increase from 275 to 310 ppbv has increased the overall loss rate, reducing the steady-state lifetime by about 1%. The more recent ozone depletion due to chlorofluorocarbons has led to similar offsets in the cumulative N_2O budget (15). On the basis of these results, the offset is small, meaning that we have consistently underestimated the anthropogenic sources of N_2O , but by only a few tenths of a teragram out of 5 TgN/year (8). More accurate estimates of this shift in the N_2O budget, and also of the latitudinal and seasonal patterns of the primary mode, need to be made from numerical experiments with the best current 2D and 3D global atmospheric chemistry models.

In summary, photochemical coupling of N_2O , NO_y , and O_3 in the stratosphere leads to a natural mode for coupled perturbations to all three species that decays 10 to 15% faster than implied from the N_2O steady-state lifetime. This pattern will be excited by emissions of N_2O or by almost any chemical perturbation, for example, those affecting stratospheric ozone. Such coupled patterns might be discernible in the atmosphere. Considering the times scales and strength of chemical coupling among the major atmospheric trace gases, this $\{N_2O, NO_y, O_3\}$ -mode is probably the longest lived perturbation of any significance to the chemical composition of the stratosphere and troposphere.

REFERENCES AND NOTES

1. M. J. Prather, *Geophys. Res. Lett.* **21**, 801 (1994).
2. ———, *ibid.* **23**, 2597 (1996).
3. W. L. Chameides and E. M. Perdue, in *Biogeochemical Cycles* (Oxford Univ. Press, Oxford, 1997), pp. 85–95.
4. M. J. Prather, *Global Biogeochem. Cycles* **11**, 393 (1997).
5. The odd-nitrogen gases (NO , NO_2 , NO_3 , N_2O_5 , $HONO$, HO_2NO_2 , and HNO_3) in the stratosphere interchange with one another but are generally conserved as a family, designated NO_y . The primary source of NO_y is from reaction of N_2O with $O(^1D)$, and the catalytic cycling of NO and NO_2 efficiently destroys O_3 in the mid-stratosphere.
6. P. J. Crutzen and D. H. Ehhalt, *Ambio* **6**, 112 (1977); S. C. Liu, R. J. Cicerone, T. M. Donahue, *Tellus* **29**, 251 (1977); M. B. McElroy, S. C. Wofsy, Y. L. Yung, *Philos. Trans. R. Soc. London Ser. A* **277**, 159 (1977).
7. R. Prinn *et al.*, *J. Geophys. Res.* **95**, 18369 (1990); M. A. K. Khalil and R. A. Rasmussen, *ibid.* **97**, 14651 (1992); T. Machida *et al.*, in *Proceedings of the International Symposium on Global Cycles of Atmospheric Greenhouse Gases*, Sendai, Japan, 7 to 10 March 1994, pp. 113–116; R. Weiss, in *ibid.*, pp. 78–80.
8. J. T. Houghton *et al.*, Eds., *Climate Change 1994, Report of the Intergovernmental Panel on Climate Change* (Cambridge Univ. Press, Cambridge, 1995), pp. 73–126.
9. D. Fisher, in *Alternative Fluorocarbons Environmental Acceptability Study (AFEAS), Proceedings of the Workshop on the Atmospheric Degradation of HCFCs and HFCs*, Boulder, CO, 17 to 19 November 1993 (AFEAS, Washington, DC, 1995), pp. 1.1–1.4.
10. Committees on Chemistry and Physics of Ozone Depletion and Biological Effects of Increased Solar UV Radiation, *Causes and Effects of Stratospheric Ozone Reduction: An Update* (National Academy Press, Washington, DC, 1982).
11. M. J. Prather and E. E. Remsberg, Eds., *Report of the 1992 Stratospheric Models and Measurements Workshop* (NASA Ref. Publ. 1292, Washington, DC, 1993).
12. In the 1D model, mixing ratios are solved at $z = 0, 4, 8, \dots, 52$ km; $p = 1000 \times 10^{-z/16}$ hPa; $N = 2.4 \times 10^{16} \times p \text{ cm}^{-3}$; and the diffusion coefficient $K = 3 \times 10^5 \text{ cm}^2 \text{ s}^{-1}$ over 0 to 12 km, $K = 3 \times 10^3 \text{ cm}^2 \text{ s}^{-1}$ at 14 km, increasing with altitude as $1/p$ (4). Chemical terms are from a detailed photochemical box model using the ATMOS 30°N chemical profiles in (7). A steady state is achieved by forcing with a surface flux of N_2O and by rapid removal of NO_y and O_3 below 12 km.
13. W. L. Chameides, S. C. Liu, R. J. Cicerone, *J. Geophys. Res.* **81**, 4997 (1976); N. D. Sze, *Science* **195**, 673 (1977).
14. C. H. Jackman *et al.*, *J. Geophys. Res.* **101**, 28753 (1996).
15. For the time between 1975 and the predicted maximum ozone depletion in the period 1995 to 2000, Charles Jackman, using the Goddard Space Flight Center 2D model, calculated a 3% drop in the instantaneous N_2O lifetime due to the greater penetration of ultraviolet sunlight to the middle stratosphere (personal communication).
16. Supported by grants from the Atmospheric Chemistry Programs of NSF and NASA to the University of California at Irvine.

23 October 1997; accepted 20 January 1998

The Role of Ocean-Atmosphere Interactions in Tropical Cooling During the Last Glacial Maximum

Andrew B. G. Bush* and S. George H. Philander

A simulation with a coupled atmosphere-ocean general circulation model configured for the Last Glacial Maximum delivered a tropical climate that is much cooler than that produced by atmosphere-only models. The main reason is a decrease in tropical sea surface temperatures, up to 6°C in the western tropical Pacific, which occurs because of two processes. The trade winds induce equatorial upwelling and zonal advection of cold water that further intensify the trade winds, and an exchange of water occurs between the tropical and extratropical Pacific in which the poleward surface flow is balanced by equatorward flow of cold water in the thermocline. Simulated tropical temperature depressions are of the same magnitude as those that have been proposed from recent proxy data.

Although the CLIMAP project (Climate: Long-Range Investigation, Mapping, and Prediction) (1) estimated that, during the Last Glacial Maximum (LGM), tropical temperatures were only modestly lower than they are today, a growing body of evidence, including corals from Barbados (2), ground water from Brazil (3), inferred snow line depressions (4), and ice cores from Peru (5), indicates that the tropics were considerably cooler. There nonetheless continues to be a debate about the extent of this cooling over the low-latitude oceans (rather than land) because some oceanic data are consistent with the CLIMAP results (6).

Simulations of LGM conditions by means of atmospheric general circulation models reproduce tropical sea surface temperatures (SSTs) that are generally consistent with the CLIMAP results. However, these models neglect oceanic motion that can affect SST. In some of the simulations (4, 7, 8), the SST is specified; in others (9, 10), the ocean is allowed only vertical mixing. Such approximations neglect oceanic upwelling, horizontal advection, and the dynamical ocean-atmosphere interactions that profoundly affect SST and that are of central importance in the following three processes: (i) Tropical ocean-atmosphere interactions of the type that causes the interannual Southern Oscillation between complementary El Niño and La Niña states (11). These interactions involve a positive feedback between the SST and the winds that causes both to amplify or attenuate. Eolian deposits and analyses of planktonic foraminifera (12–14), which indicate that

A. B. G. Bush, Department of Earth and Atmospheric Sciences, 126 Earth Sciences Building, University of Alberta, Edmonton, Alberta, Canada T6G 2E3.
S. G. H. Philander, Department of Geosciences, Guyot Hall, Princeton University, Princeton, NJ 08544, USA.

*To whom correspondence should be addressed. E-mail: andrew.bush@ualberta.ca

the low SST during the LGM was associated with an intensification of the trade winds and an increase in the slope of the thermocline, are consistent with these interactions. The type of ocean-atmosphere interactions that result in El Niño involves an adiabatic, east-west redistribution of warm surface waters in the equatorial Pacific that leaves the structure of the mean thermocline unchanged and has a time scale of a few years at most (15). (ii) Processes that can affect the thermocline itself, on decadal time scales. These processes include a shallow, wind-driven, tropical-extratropical, oceanic exchange in which poleward flow in the surface layers subducts in the subtropics, returns to low latitudes in the thermocline, and wells up at the equator (16). A decrease in SST of the extratropics in due course lowers the temperature of the water that subducts in the subtropics and subsequently alters the properties of the equatorial thermocline, thus influencing ocean-atmosphere interactions in low lati-

tudes. (iii) The thermal structure of the deep ocean. This structure, on time scales of centuries and longer, depends on the thermohaline circulation that involves the sinking of cold, saline waters in certain high latitudes. The calculations to be described here simulate LGM conditions for a few decades at most so that processes (i) and (ii) are included but process (iii) is excluded. The thermal structure of the upper ocean, which depends on processes (i) and (ii), adjusts to LGM conditions, but that of the deep ocean remains close to the initially prescribed modern conditions.

We developed a fully coupled general circulation model of the atmosphere and ocean (17) in which the oceanic component permits motion in all three directions and the coupling scheme permits dynamical ocean-atmosphere interactions. The model domain is global and has, in the spectral atmospheric model, an equivalent spatial resolution of 2.25° in latitude by 3.75° in longitude. In the grid-point ocean model,

the resolution is 2.00° in latitude by 3.62° in longitude. There are 14 and 15 vertical levels in the atmospheric and oceanic models, respectively. To simulate the LGM, we specified the following quantities: orbital parameters appropriate to 21,000 years before present to govern seasonal insolation, 200 parts per million atmospheric CO₂, ice sheet topography (18), glacial albedo (1), and glacial sea level (19). The time integration proceeds asynchronously at 1-day intervals; at the end of each day, the daily mean values of SST and surface currents are passed as boundary conditions to the atmospheric model, and those of the wind stress, net heat flux, net freshwater flux, and net shortwave radiation are passed to the oceanic model.

Before proceeding to the LGM simulation, we performed a 40-year integration for the present-day climate, starting from Levitus's data (20) for the ocean, without applying any flux corrections to the model. The simulated climatology is reasonable except that the predicted amount of stratus cloud, as parameterized in (21), is too low in the eastern equatorial Pacific, so SST is higher than for the observed climatology in this region (Fig. 1A). In the LGM simulation, which also starts from Levitus's data, the initial, rapid atmospheric adjustments (within weeks) to the glacial forcing (including lower atmospheric CO₂ concentrations) are a decrease in temperature, substantial changes in the direction and speed of the midlatitude westerly jets, and intensification of the trade winds. Up to this stage, the simulation is in accord with earlier simulations (8, 9), but the adjustment in our model then continues in two more steps (Fig. 2): first, during the first year, a sharp drop in equatorial temperatures and a further intensification of the trade winds, all part of process (i), and, next, a gradual decrease in temperatures over a period of several years in response to process (ii), which allows extratropical surface conditions to affect the equatorial thermocline and hence the ocean-atmosphere interactions.

When the simulated SSTs for today's climate are subtracted from those for the LGM (Fig. 1B), SST cooling on the order of 2° to 3°C can be seen over large parts of the globe (underneath the subtropical highs, for example). This cooling can be accounted for by the reduced atmospheric CO₂ and the glacial boundary forcing, as in earlier models (9, 10). In our model, the extratropical cooling lowers temperatures in the equatorial thermocline over the next decade of simulation (because of the shallow, meridional, wind-driven circulation described above) and affects ocean-atmosphere interactions. Those interactions are primarily responsible for the tropical cooling of 4° to 6°C in the western

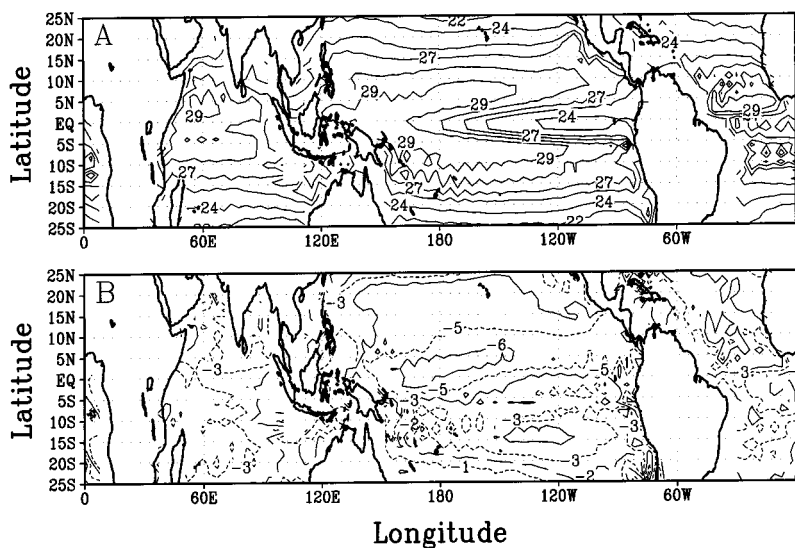
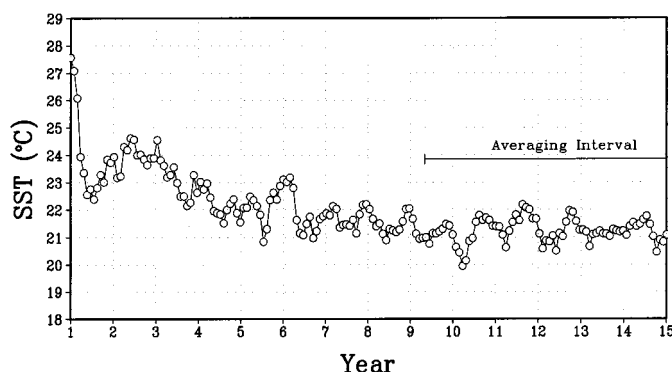


Fig. 1. (A) Annual mean SST (in degrees Celsius) in the present-day simulation (averaged over the past 23 years; the contour interval is 1°C for temperatures above 26°C and 2°C for temperatures below 26°C). (B) The SST difference (LGM, averaged over the past 5 years, minus present day). The contour interval is 1°C with odd values contoured with short dashes and even values contoured with a solid line. The -2°C isotherm is contoured with long dashes for clarity. EQ, equator.

Fig. 2. Time series of SST on the equator averaged between 180°E and 140°W for the LGM simulation. Open circles represent monthly mean values. The 5-year averaging interval over which annual mean results are obtained for the LGM is indicated.



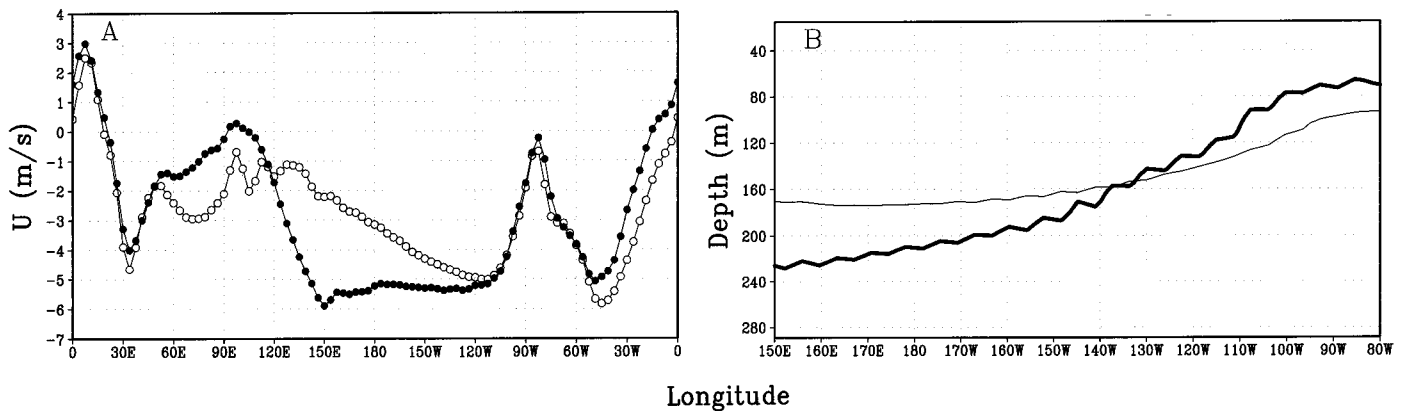


Fig. 3. (A) Simulated annual mean zonal wind U averaged from 10°S to 10°N as a function of longitude in present day (open circles) and the LGM (solid circles). (B) Simulated depth of the 18°C isotherm in the Pacific Ocean in

present day (thin line) and the LGM (thick line). (The longitude scales in the two figures are not the same.)

Pacific, the strengthening of the trade winds (Fig. 3A), the enhancement of the tilt of the thermocline (Fig. 3B), and the increase in the peak speeds of the South Equatorial Current and the Equatorial Undercurrent by a factor of nearly 2. These changes translate into stronger upwelling and zonal advection, processes that amount to an additional cooling (relative to today) of 18.6 W/m² of the upper equatorial ocean. To compensate, there is an increase in shortwave radiation over the western Pacific because the region of strong convection shifts westward over the Indonesian archipelago. There the latent heat release produces what looks like a baroclinic response in the mean zonal circulation (22) that feeds back on the Pacific easterlies. In Fig. 4, the anomalous LGM heating is the region of minimal cooling above the surface near 100°E; the enhanced surface easterlies are most likely a combined response to both the shift in convection and an increased flux of easterly momentum from midlatitude baroclinic waves.

In a zonal mean, atmospheric temperatures in the high northern latitudes are 6° to 8°C colder throughout the entire troposphere, whereas tropical tropospheric temperatures are 4° to 6°C lower (the colder values occur in the upper equatorial troposphere and arise from a decrease in latent heat release). Glacial forcing therefore amplifies the atmosphere's meridional baroclinic structure: The vertical shear in zonal winds in the North Atlantic storm track is 26% greater. This amplification would increase the frequency with which baroclinic eddies are spawned (23) and, as has already been demonstrated for the LGM (8), increases the eddy fluxes of heat and momentum. Evidence for this increase is in the strength of the Northern Hemisphere Hadley cell, which is, in the LGM simulation, 20% greater.

Mean annual atmospheric temperature

depressions in the lowest model level (about 30 m above ground in a standard atmosphere) indicate more than 7°C cooling over the East African Highlands and Central America and 5°C cooling over much of the tropical Pacific Ocean. Continental interiors in the tropics are, in general, 5° to 6°C colder with a fair amount of spatial variability. The LGM atmosphere is 4.3°C colder near the surface (globally averaged). The glacial cooling is not as large, however, over the high-latitude Southern Hemisphere oceans, although temperature depressions in the central Antarctic reach 11°C. Differential cooling of the Northern and Southern Hemispheres in response to the LGM ice sheet distribution has been noted in previous studies (9, 24).

The globally averaged surface temperature of a planet depends primarily on two factors: the albedo and the atmospheric concentration of greenhouse gases. The var-

ious simulations of the LGM, including this one, all take into account the high albedo associated with glaciers and low atmospheric concentration of CO₂. Part of the explanation for the lower temperatures in this simulation (relative to earlier simulations) is a decrease in the concentration of another greenhouse gas, water vapor. Simulated global mean LGM specific humidity is 10% less than in the present-day simulation. (Relative humidity, however, increases by 5% because the net decrease in saturation vapor pressure induced by colder temperatures is greater than the net decrease in specific humidity.) During the simulated LGM, the hydrological cycle is weaker than today; both evaporation and precipitation are reduced by about 10%.

Although the simulations described here are in short-term equilibrium (Fig. 2), further changes are likely on time scales of centuries when the thermohaline circula-

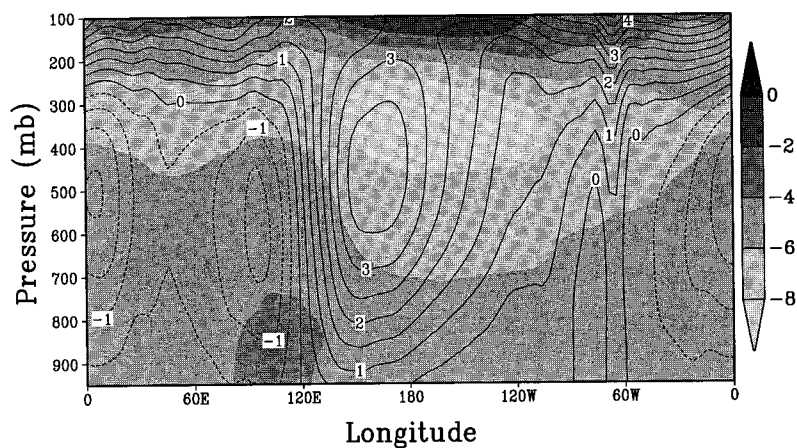


Fig. 4. Difference in annual mean temperature (shaded) as a function of longitude and height [950 to 100 mbar (mb)] averaged between 30°S and 30°N (LGM minus present day; quantities are temporally averaged as in Fig. 1). The bar on the right gives the scale (in degrees Celsius). Superposed in contours is the difference in the mean Walker circulation averaged between 30°S and 30°N (contour interval is 0.5×10^{11} kg/s).

tion alters the thermal structure of the deep ocean (25). Calculations for such extended periods are beyond the scope of this study.

REFERENCES AND NOTES

1. Climate: Long-Range Investigation, Mapping, and Prediction (CLIMAP) Project Members, *Map and Chart Series MC-36* (Geological Society of America, Boulder, CO, 1981).
2. T. P. Guilderson, R. G. Fairbanks, J. L. Rubenstone, *Science* **263**, 663 (1994).
3. M. Stute *et al.*, *ibid.* **269**, 379 (1995).
4. D. Rind and D. Peteet, *Quat. Res.* **24**, 1 (1985).
5. L. G. Thompson *et al.*, *Science* **269**, 46 (1995).
6. W. S. Broecker, *Quat. Res.* **26**, 121 (1986); M. W. Lyle, F. G. Prahl, M. A. Sparrow, *Nature* **355**, 812 (1992).
7. J. E. Kutzbach and P. J. Guetter, *J. Atmos. Sci.* **43**, 1726 (1986).
8. N. M. J. Hall, P. J. Valdes, B. Dong, *J. Clim.* **9**, 1004 (1996).
9. S. Manabe and A. J. Broccoli, *J. Geophys. Res.* **90**, 2167 (1985).
10. A. J. Broccoli and S. Manabe, *Clim. Dyn.* **1**, 87 (1987).
11. S. G. H. Philander, *El Niño, La Niña, and the Southern Oscillation*, vol. 46 of *International Geophysics Series* (Academic Press, New York, 1990); J. D. Neelin, M. Latif, F.-F. Jin, *Annu. Rev. Fluid Mech.* **26**, 617 (1994).
12. D. Andreasen and C. Ravelo, *Paleoceanography* **12**, 395 (1997).
13. T. F. Pederson, *Geology* **11**, 16 (1983).
14. See a summary by T. J. Crowley and G. R. North [*Paleoclimatology* (Oxford Monograph on Geology and Geophysics 18, Oxford Univ. Press, New York, 1991)], pp. 56–57.
15. The horizontal redistribution of warm surface waters during El Niño alters the topography of the thermocline—it deepens in some regions and shoals in others—while leaving unchanged the spatially averaged depth of and the temperature difference across the thermocline. That is why two-layer models of the ocean are effective tools for studying El Niño.
16. Z. Liu and S. G. H. Philander, *J. Phys. Oceanogr.* **25**, 449 (1995); D. Gu and S. G. H. Philander, *Science* **275**, 805 (1997).
17. C. T. Gordon and W. Stern, *Mon. Weather Rev.* **110**, 625 (1982); R. C. Pacanowski, K. Dixon, A. Rosati, "The GFDL Modular Ocean Model user guide," *GFDL Ocean Group Tech. Rep. 2* (Geophysical Fluid Dynamics Laboratory, Princeton, NJ, 1991).
18. W. R. Peltier, *Science* **265**, 195 (1994).
19. R. G. Fairbanks, *Nature* **342**, 637 (1989).
20. S. Levitus, *NOAA Prof. Pap. 13* (U.S. Government Printing Office, Washington, DC, 1982).
21. S. G. H. Philander *et al.*, *J. Clim.* **9**, 2958 (1996).
22. A. E. Gill, *Q. J. R. Meteorol. Soc.* **106**, 447 (1980).
23. A. B. G. Bush and W. R. Peltier, *J. Atmos. Sci.* **51**, 1581 (1994).
24. W. T. Hyde, T. J. Crowley, K.-Y. Kim, G. R. North, *J. Clim.* **2**, 864 (1989).
25. D. P. Schrag, G. Hampt, D. W. Murray, *Science* **272**, 1930 (1996).
26. This work was supported by a Natural Sciences and Engineering Research Council of Canada grant OGP0194151 (A.B.G.B.) and by the National Oceanic and Atmospheric Administration under contract NOAA-NA56GP0226 (S.G.H.P.). We thank the staff of the Geophysical Fluid Dynamics Laboratory for making this work possible.

7 November 1997; accepted 20 January 1998

Molecular Mimicry by Herpes Simplex Virus-Type 1: Autoimmune Disease After Viral Infection

Zi-Shan Zhao, Francesca Granucci, Lily Yeh, Priscilla A. Schaffer,* Harvey Cantor

Viral infection is sometimes associated with the initiation or exacerbation of autoimmune disease, although the underlying mechanisms remain unclear. One proposed mechanism is that viral determinants that mimic host antigens trigger self-reactive T cell clones to destroy host tissue. An epitope expressed by a coat protein of herpes simplex virus-type 1 (HSV-1) KOS strain has now been shown to be recognized by autoreactive T cells that target corneal antigens in a murine model of autoimmune herpes stromal keratitis. Mutant HSV-1 viruses that lacked this epitope did not induce autoimmune disease. Thus, expression of molecular mimics can influence the development of autoimmune disease after viral infection.

Autoimmune diseases result from a loss of self-tolerance and the consequent immune destruction of host tissues (1). Although the pathology of the associated tissue destruction has been well characterized, the

mechanisms responsible for initiation and pathogenesis of autoimmune diseases remain unclear. Several mechanisms have been proposed on the basis of the clinical observation that viral infections can induce or exacerbate autoimmune disease (2). Virus-induced inflammatory responses that result in release of self antigens and enhancement of costimulatory activity may trigger autoreactive T cells (3, 4). It also has been proposed that viral determinants that mimic host antigens directly stimulate self-reactive T cell clones to attack sequestered host

tissues (5). Certain viral peptides that cross-react with self peptides can stimulate autoreactive T cells (6), and mice genetically engineered to express a viral protein can develop autoimmune disease after infection with the relevant virus (7). However, these observations do not provide direct evidence that viral infection can precipitate autoimmune disease by mechanisms that include molecular mimicry. Herpes stromal keratitis (HSK), a disorder induced by HSV-1 infection and characterized by T cell-dependent destruction of corneal tissue, is a leading cause of human blindness (4, 8). To examine the role of viral mimicry in autoimmune disease, we have now studied a murine model of HSK in which corneal HSV-1 infection reproducibly results in a T cell-mediated autoimmune reaction (8, 9).

Murine HSK elicited by HSV-1 (KOS strain) in C.AL-20 mice is mediated by CD4⁺ T cell clones specific for corneal self antigens but that also recognize a peptide (amino acids 292 to 308) in the C_H3 region of immunoglobulin G2a^b (IgG2a^b) (9). However, the role of this virus in the induction of HSK disease was not investigated. Given that there are insufficient numbers of T cells in the cornea after HSV-1 (KOS) infection to define potentially cross-reactive cells (10), we investigated whether the HSK-inducing C1-6 and C1-15 T cell clones might also recognize HSV-1 epitopes by measuring their proliferative response after stimulation with HSV-1 antigens. Both HSK-inducing clones, but not the ovalbumin (OVA)-reactive clone O3 (11), were activated by extracts of HSV-1 (KOS)-infected Vero cells [10⁵ ultraviolet (UV)-inactivated plaque-forming units (PFU) per milliliter] but not by extracts of uninfected Vero cells (Fig. 1A).

We searched the GenBank database for HSV-1 proteins that share sequence homology with the keratogenic peptide recognized by C1-6 and C1-15. The best match was with a peptide sequence embedded in the HSV virion-associated protein UL6 (12), which contains identical or similar amino acids at seven of eight sequential positions that contribute to T cell recognition (Arg-Lys-Ser-Asp-Ser-Glu-Arg-Gly; mismatched residue in italics) (9). Both keratogenic clones, but not the OVA-reactive clone, were activated by a synthetic 15-residue viral peptide based on UL6 (amino acids 299 to 314) [UL6-(299–314)] and containing this nested sequence, whereas an unrelated peptide derived from murine mammary tumor virus (MMTV) did not activate these two clones at any concentration tested (Fig. 1B).

The proliferative response of the two keratogenic CD4⁺ T cell clones to the UL6-(299–314) peptide suggested that in-

Z.-S. Zhao, F. Granucci, H. Cantor, Department of Pathology, Harvard Medical School, and Department of Cancer Immunology and AIDS, Dana-Farber Cancer Institute, Boston, MA 02115, USA.

L. Yeh and P. A. Schaffer, Division of Molecular Genetics, Dana-Farber Cancer Institute, Boston, MA 02115 USA.

*Present address: Department of Microbiology, University of Pennsylvania School of Medicine, Philadelphia, PA 19104 USA.